Available online at www.sciencedirect.com
ScienceDirect
International Journal of Multiphase Flow 34 (2008) 241–259
International Journal of Multiphase Flow
www.elsevier.com/locate/ijmulflow

Bag breakup of nonturbulent liquid jets in crossflow

C.-L. Ng, R. Sankarakrishnan, K.A. Sallam *

School of Mechanical and Aerospace Engineering, 218 Engineering North, Oklahoma State University, Stillwater, OK 74078-5016, USA

Received 21 September 2006; received in revised form 7 June 2007

Abstract

An experimental investigation of the bag breakup of round nonturbulent liquid jets in gaseous crossflow at room temperature and pressure is described. Pulsed photography, pulsed shadowgraphy, and high-speed imaging were used to observe the column and surface waves along the liquid jet and the formation and breakup of bags. Measurements included: wavelengths of column and surface waves, jet velocities, the number of bags along the liquid jet, the number of nodes per bag, droplets sizes and velocities, and trajectories of droplets. Present results show that the column waves of a nonturbulent liquid jet in crossflow within bag breakup regime can be explained based on Rayleigh–Taylor instability. The number of nodes per bag affected the breakup mechanism of the bags. Three distinctive sizes of droplets were produced due the breakup of the bag membrane, the ring strings and the ring nodes. The size of the droplets resulting from the breakup of the bag membrane was constant independent of the crossflow Weber number. Finally different trajectories were observed for the three groups of droplets.

Keywords: Jet breakup; Atomization; Sprays; Drop; Crossflow; Rayleigh–Taylor

1. Introduction

The wave phenomena and breakup outcomes of round nonturbulent liquid jets in uniform gaseous crossflow within the bag breakup regime were studied experimentally, motivated by applications to spray breakup in crossflow in air-breathing propulsion systems, liquid rocket engines, and agricultural sprays, among others. Earlier *studies* of round nonturbulent liquid jets in uniform gaseous crossflow had focused on lengths of penetration of the liquid jet and jet trajectories for various liquid jet and crossflow properties (Geary and Margettes, 1969; Kitamura and Takahashi, 1976; Schetz and Padhye, 1977; Less and Schetz, 1986; Nguyen and Karagozian, 1992; Inamura, 2000; Madabhushi, 2003; Birouk et al., 2003, 2007; Iyogun et al., 2006; Ryan, 2006). Air density effects on the penetration and trajectories were investigated by Becker and Hassa (2002), Cavaliere et al. (2003), Stenzler et al. (2006), Bellofiore et al. (2007) and Ragucci et al. (2007).

Recently, primary breakup mechanism was studied by Wu et al. (1997), Vich (1997), and Mazallon et al. (1999) who reported that nonturbulent liquid jets in crossflow can experience bag, multimode and shear breakup similar to the secondary breakup of drops. The breakup regime transitions were identified by Wu et al. (1997) who constructed a breakup regime map of liquid jets in crossflow using the crossflow Weber number, $We_G = \rho_G d_j U_G^2/\sigma$ (where ρ_G and U_G are the crossflow gas density and velocity, respectively, d_j is the liquid jet exit diameter, and σ is the surface tension), and the momentum flux ratio, $q = \rho_L v_j^2/\rho_G U_G^2$ (where ρ_L is liquid density and v_j is the jet exit velocity) as the map coordinates. Mazallon et al. (1999) observed, however, that for low Ohnesorge number, $Oh = \mu_L/[\rho_L \sigma d_j]^{1/2} < 0.1$ (where μ_L is the liquid dynamic viscosity), the breakup regime transitions are controlled by the crossflow Weber number alone. Mazallon et al. (1999) constructed a new breakup regime maps in terms of the crossflow flow Weber number and the Ohnesorge number as the map coordinates. Later, Sallam et al. (2004) modified the boundary for the transition between the bag breakup regime and the multimode breakup

* Corresponding author. Tel.: +1 405 762 0749; fax: +1 405 744 7873.
E-mail address: khaled.sallam@okstate.edu (K.A. Sallam).

0301-9322/$ - see front matter © 2007 Elsevier Ltd. All rights reserved.
doi:10.1016/j.ijmultiphaseflow.2007.07.005

regime. Aalburg et al. (2005) found that for the large Ohnesorge number the deformation of the jet is controlled by a new dimensionless number, $We_G^{1/2} \times Oh$, and constructed a breakup regime map for large Oh jet using $We_G^{1/2} \times Oh$ and $1/Oh$ as the map coordinates.

The location of the fracture point for nonturbulent liquid jets in crossflow was studies by Wu et al. (1997) who reported that the breakup cross-stream location for the three breakup regimes, bag, multimode, and shear, was constant and equal to 8 jet diameters whereas the streamwise breakup location was found to depend on the momentum flux ratio. Sallam et al. (2004) observed that the breakup time for low Ohnesorge number jets was independent of the Weber number for the three breakup regimes and was $2.5t^*$, where t^* is the aerodynamic characteristics time ($t^* = d_j(\rho_L/\rho_G)^{1/2}/U_G$) due to Ranger and Nicholls (1969). Despite these similarities the bag and shear breakup regimes are quite different regarding the jet deformation prior to the onset of breakup, the breakup mechanism, and the jet trajectory. For multimode and shear breakup regimes Sallam et al. (2004) measured the drops and ligaments sizes, drop velocities, and rates of breakup for the multimode and shear breakup, but these measurements were not conducted within the bag breakup regime.

The objectives of the present investigation were to extend the recent experimental studies of Mazallon et al. (1999) and Sallam et al. (2004) in the bag breakup regime by observing the upwind and downwind liquid jet surfaces, column and surface waves, the temporal evolution and breakup of bags, and the breakup outcomes: droplets sizes and velocities after the breakup, and trajectories of liquid droplets. Finally, phenomenological analyses were used to help interpret and correlate the measurements.

2. Experimental methods

2.1. Apparatus

The present study employed pulsed photography, single- and double-pulsed shadowgraphy, and high-speed imaging to investigate the breakup of round nonturbulent liquid jets injected in a subsonic wind tunnel for various test condi-

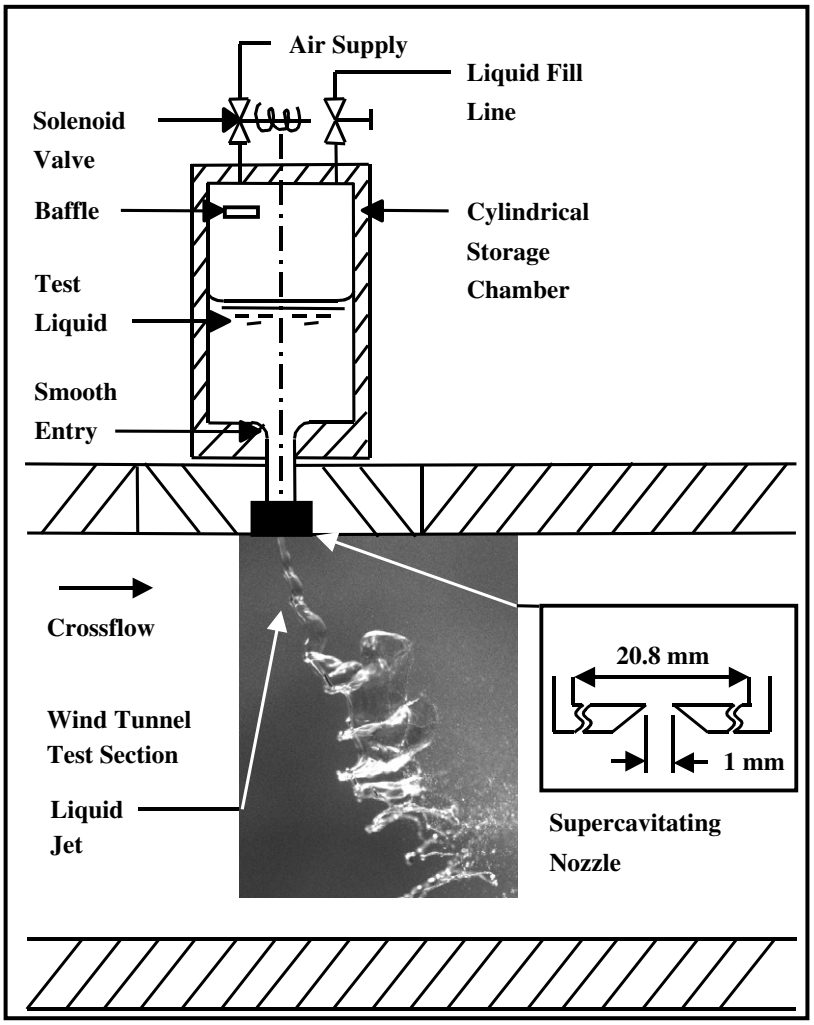

Fig. 1. Test apparatus.

tions. The schematic of the injection system employed to generate the round nonturbulent liquid jets in this study is shown in Fig. 1. Pressure injection was used to feed the test liquids stored in a type 304 stainless steel cylindrical storage chamber (diameter = 100 mm and height = 150 mm) through a supercavitating nozzle directed vertically downward into the test section of a subsonic wind tunnel (0.3 m × 0.3 m × 0.6 m) at room temperature and atmospheric pressure. The supercavitating nozzle had a sharp-edged inlet and internal to exit diameter ratio greater than 20 (Fig. 1) to generate a round nonturbulent liquid jet. Pressurized air was admitted to the top of the chamber through a solenoid valve to force the test liquid out of the supercavitating nozzle. A baffle at the air inlet prevented excessive aeration of the test liquid during injection. The pressurized air was stored on the upstream side of the solenoid valve in an accumulator tank (volume = 0.18 m^3). The injector was flush-mounted with the ceiling of the wind tunnel test section. The duration of the liquid jet injection was greater than 33 s which was long compared to the 8–157 ms flow development times. The open circuit wind tunnel had a contraction ratio greater than 16:1. The wind tunnel test section has optical quality glass sidewalls and floor, and acrylic ceiling to provide optical access to the test section. The test section was designed to provide a clear view of the jet exit. The air velocity in the test section, U_G, was measured by a Pitot-Static tube (United Sensors Model PDC-18-G-16-KL) fitted to the end of the test section at the centerline. The Pitot-Static tube was connected to an inclined tube 0-10″ H_2O manometer (Dwyer Model No. 400-10-Kit) through two clear plastic tubes. The test section velocities ranged from 3 m/s to 60 m/s with a velocity variation across the test section of less than ±1%. The turbulence level inside the test section was measured by the manufacturer of the wind tunnel (ELD, Inc.) to be less than 0.25%.

2.2. Instrumentation

Pulsed photography, single- and double-pulsed shadowgraphy, and high-speed imaging were used to observe round nonturbulent liquid jets in uniform gaseous crossflow under various test conditions to investigate the wave

Table 1
Liquid properties and test conditions[a]

Liquid	Water	Ethyl alcohol
Density, ρ_L, kg/m^3	997	809
Crossflow velocity, U_G, m/s	10–60	13–35
Jet exit velocity, V_j, m/s	7–50	10–40
Liquid/gas density ratio, ρ_L/ρ_G	821	665
Liquid viscosity, kg/m s × 10^{-4}	8.94	12.3
Liquid/gas viscosity ratio, μ_L/μ_G	48	66
Surface tension, N/m × 10^{-3}	70.8	27
Nozzle exit diameter, mm	0.5, 1.0, and 2.0	0.5 and 1.0
Crossflow Weber number, We_G	4–30	8–28
Crossflow Reynolds number, Re_G	709–3818	876–1638
Momentum flux ratio, q	9–1199	52–902
Liquid jet Ohnesorge number, $Oh \times 10^{-3}$	<4.8	<11.8

[a] Air crossflow at room temperature and pressure.

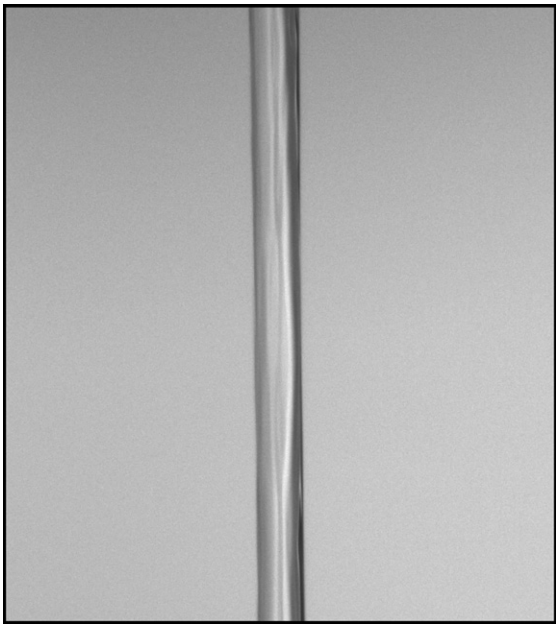

Fig. 2. A round nonturbulent liquid jet in still air (water jet, $d_j = 1$ mm, $We_G = 0$, $Re_L = 30{,}000$, and $q = \infty$).

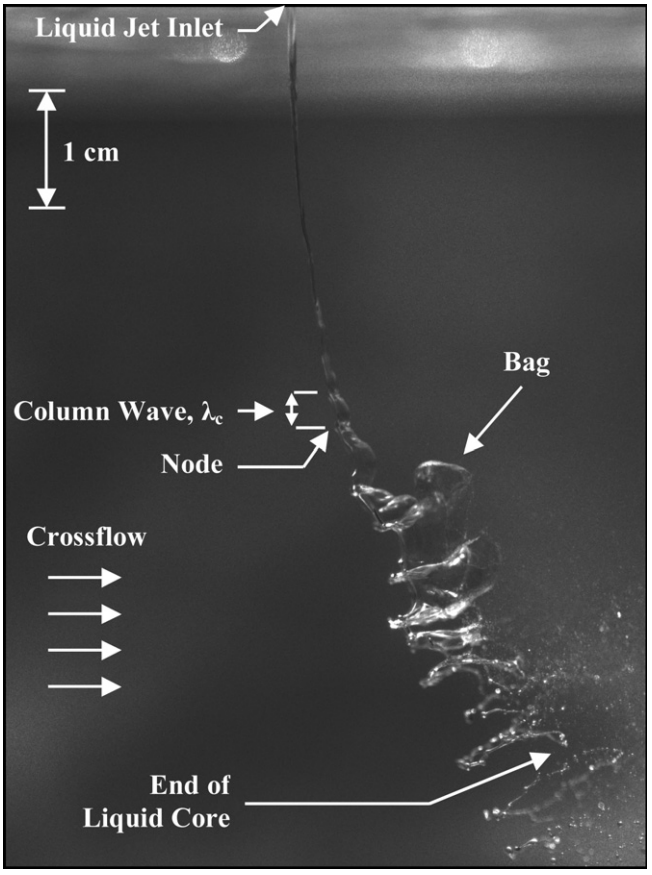

Fig. 3. A round nonturbulent liquid jet in uniform gaseous crossflow within the bag breakup regime (ethyl alcohol jet, $d_j = 1$ mm, $We_G = 10$, and $q = 224$).

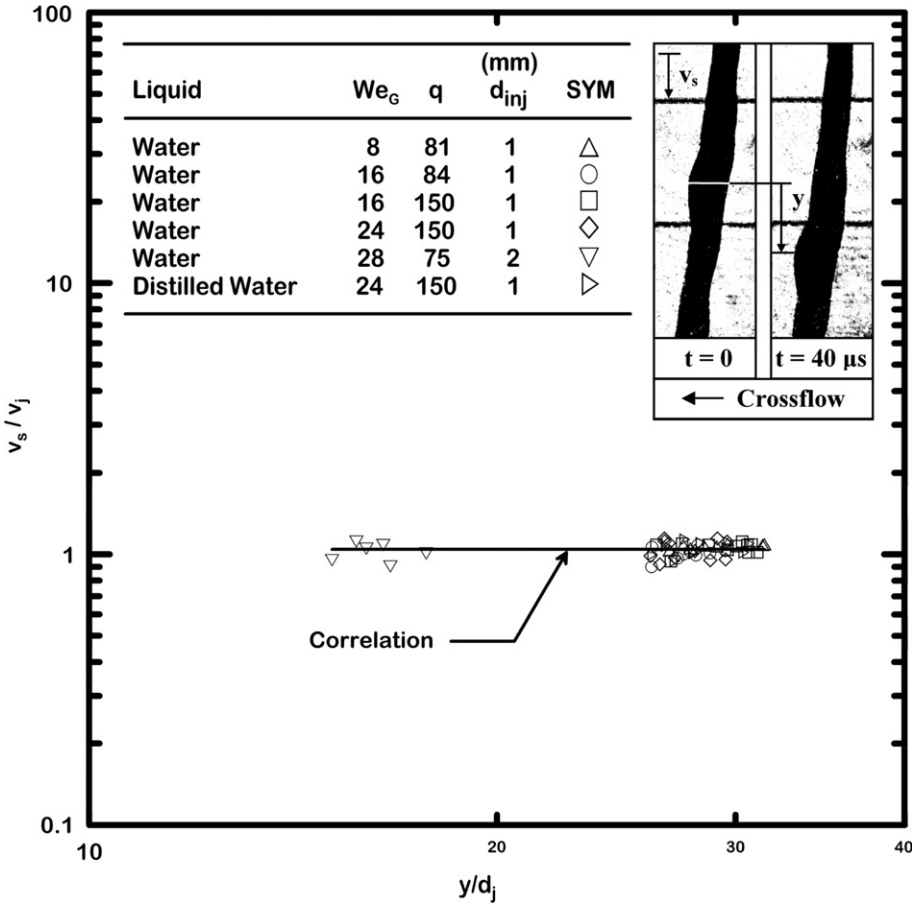

Fig. 4. Streamwise jet surface velocity as a function of streamwise distance.

phenomena, breakup mechanisms, and droplets properties. Pulsed photography was employed to measure the wavelengths of column and surface waves, number of bags along the liquid jet, and the trajectories of the droplets. The light source for pulsed photography was a frequency-doubled Nd:YAG laser (Spectra Physics, Model: LAB-150) that generated a light pulse with energy up to 300 mJ/pulse at 532 nm. The beam energy was controlled by an external half waveplate (Thorlabs, Model: WPMH05M-532). The laser beam was expanded by an objective lens (Newport, Model: M-20X) to illuminate the liquid jet through the glass floor of the wind tunnel test section. The images were recorded using a CCD camera (Cooke, Model: PCO 2000) that has 2048 × 2048 pixels CCD sensor equipped with a camera lens (Nikon, Model: D-AF Micro-Nikkor 105 mm f/2.8). The camera was normal to the plane of symmetry of the wind tunnel for all of the aforementioned investigations except when observing the downwind surface waves where the camera was tilted 40° in the downwind direction from the normal position to the crossflow.

Pulsed shadowgraphy was employed to measure the sizes of the droplets. The beam energy of the Nd:YAG laser was controlled by an external half waveplate. The laser beam was expanded by an objective lens (Newport, Model: M-5X) and spatial filter and then collimated by a positive lens (Newport, Model: KPX226AR.14) and was used to illuminate the liquid jet through the glass sidewall of the wind tunnel test section. A relay lens (Newport, Model: KPX232AP.14) was used on the opposite side of the glass sidewall and the resulting image was constructed at the CCD camera instrumented with a bellow expander (Nikon, Model: PB-6).

Double-pulsed shadowgraphy was used to measure the surface velocity of the liquid jet and the velocities of the droplets after the breakup. The same setup as single-pulsed shadowgraphy was used except for using two laser pulses from two independent lasers heads. The time delay between the two pulses was controlled by a delay generator (Quantum Composers, Model: 9518, with a resolution of 100 ns) and was varied in the range of 40–120 μs based on the test conditions. Two full resolution images were recorded on the CCD camera which was operating in the double-exposure mode with an inter-frame time as small as 400 nm. The velocities of the liquid jet surface and the droplets were computed by measuring the distances traveled by the irregularities on the liquid surface or by the centroid of a certain droplet between the two *pulses. For all shadowgraphy and photography measure-*

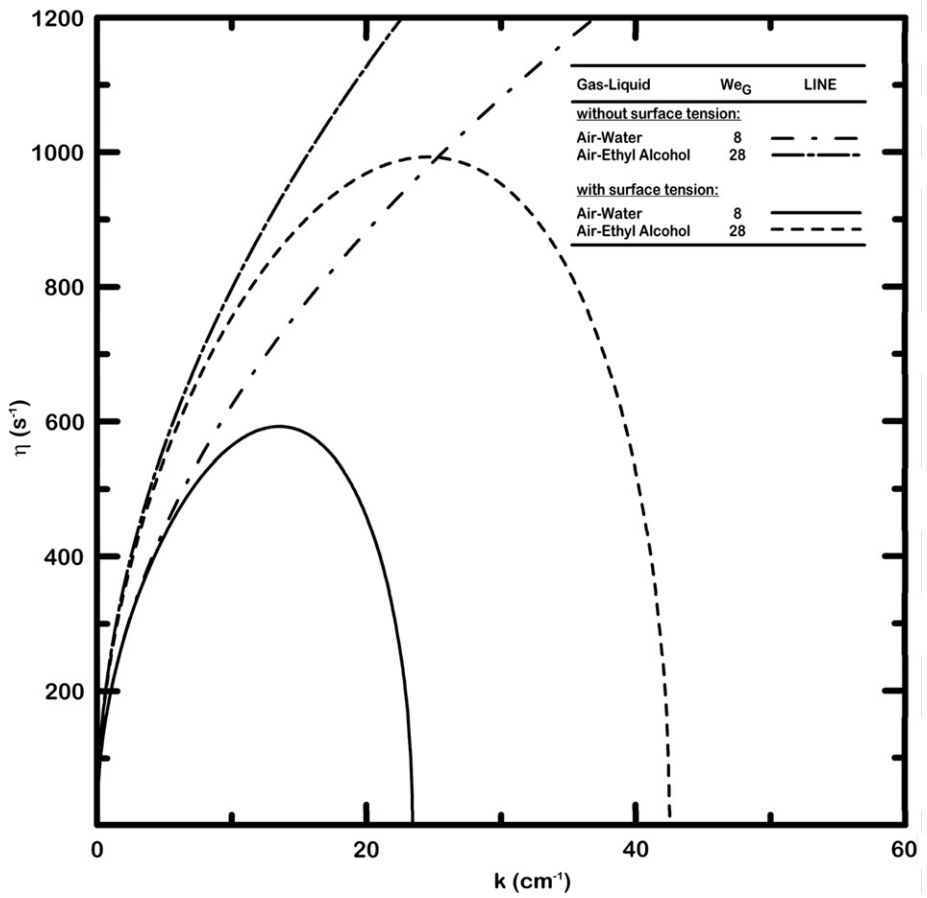

Fig. 5. Growth rate of Rayleigh–Taylor instabilities as a function of wave numbers with and without the effects of the surface tension. [(a) water jet, $d_j = 1$ mm, $We_G = 8$, and (b) ethyl alcohol jet, $d_j = 1$ mm, $We_G = 28$]

ments, the camera was operated with an open shutter under dark room conditions and the exposure time was controlled by the duration of the laser pulse (<7 ns).

High-speed imaging was used to observe the temporal evolution and breakup of the bags. A high-speed camera (IDT, Model: XS-4) with a 512 × 512 CMOS sensor was used to record the images at 5145 frames per second at full resolution. Two halogen bulbs (Sylvania Model: 58865 double-ended 500 W) provided continuous light source for the high-speed imaging. To observe the upwind surface of the liquid jet, the camera was tilted 13° in the upwind direction from the normal position to the crossflow.

The resulting images were analyzed using the Sigma-Scan Pro5 software. No filtering or digital image enhancement techniques were needed. Irregular drops were assumed to be elliptic and were assigned diameters equal to the diameter of the circle having the same area as the ellipse. Except for effects of this definition of drop diameters, which are difficult to quantify, experimental uncertainties for drop diameters as small as 43 μm were within 10% uncertainties (at 95% confidence). Measurements of the Sauter mean diameter, $SMD = \Sigma d^3/\Sigma d^2$, were obtained by summing over 50 ± 200 droplets at each condition to obtain experimental uncertainties (95% confidence) less than 30%, mainly dominated by sampling limitations. Measurements of liquid surface velocities were based on the measuring the displacements of particular points along the surface (wave crest) and other surface irregularities using double-pulsed imaging. Over 50 ± 200 points were used to yield average surface velocities with experimental uncertainties (95% confidence) less than 10%, dominated by sampling limitations. Drop velocities were measured in the same way to yield experimental uncertainties (95% confidence), as follows: node-droplets and ring-droplets velocities less than 15% (95% confidence level), and bag-droplets velocities less than 35% (95% confidence level) due to sampling limitations. The nozzle exit velocity, v_j, was measured by measuring the collected volume of injected test liquid over a specific time period. In all cases, the velocity measurements were repeated over 30–100 times to achieve measurements uncertainties smaller than 10% (95% confidence level). The trajectories of the droplets were not based on the tracking of each single droplet in the spray but rather based on averaging the height, y, of the droplets at a particular downstream location, x, from many images. The number of images used, 50–200 were selected to achieve uncertainties less than 10% within 95% confidence level.

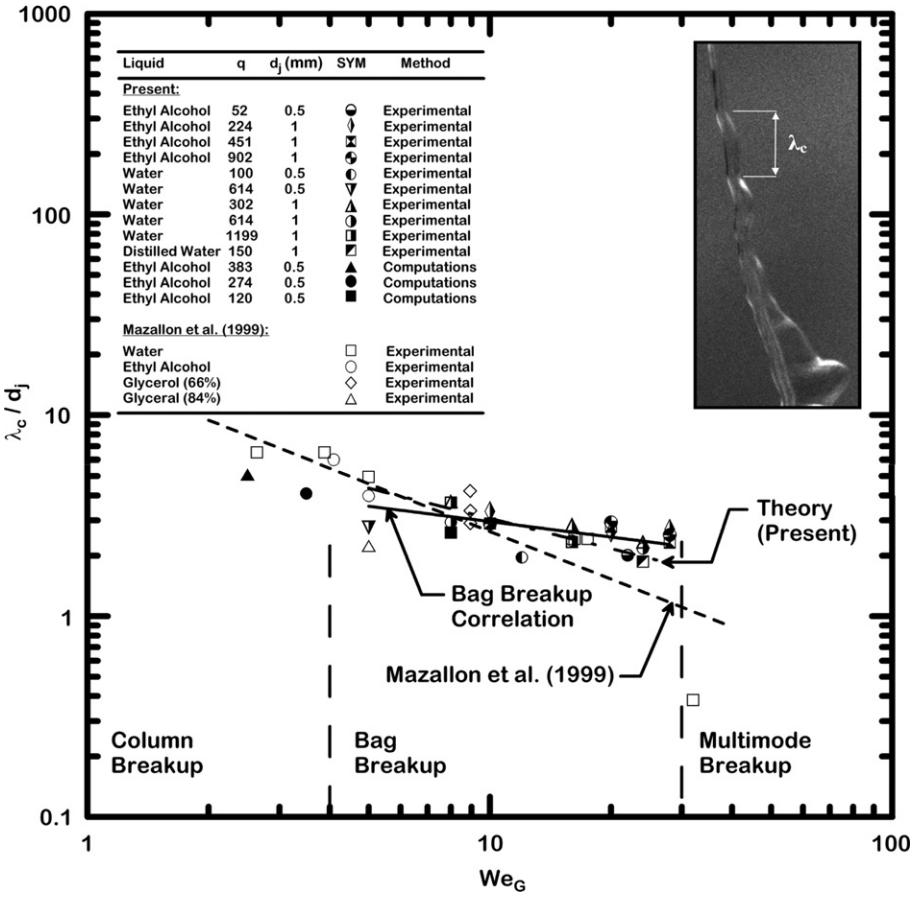

Fig. 6. Wavelengths of column waves as a function of crossflow Weber number.

2.3. Test conditions

The test conditions are summarized in Table 1. The test liquids are tap water (referred herein as water), and ethyl alcohol. The liquid properties were measured as follows: liquid density, ρ_L, using a set of hydrometers (Fisher model 11-582), liquid kinematic viscosity, ν_L, using a Cannon-Fenske viscometer (Fisher model 13-617y) and surface tension, σ, using a ring tensiometer (Fisher model 20). For water liquid jet nozzle exit diameters, d_j, of 0.5, 1.0, and 2.0 mm were employed to study a crossflow Weber number variation from 4 to 30 and momentum flux ratio variation from 9 to 1199. For ethyl alcohol jet nozzle exit diameters of 0.5 and 1.0 mm were used to study a liquid jet Weber number in the range from 8 to 28 and a momentum flux ratio ranging from 52 to 902. For all cases, the liquid jet Ohnesorge numbers were small (<0.1).

3. Results and discussion

3.1. Flow visualization

Pulsed photograph of a typical round nonturbulent liquid jet in still air is shown in Fig. 2. The water jet presented herein has a diameter of 1 mm and a nozzle exit mean velocity of 27 m/s. The liquid jet exhibits a smooth surface with no initialization of surface breakup even though the jet Reynolds number ($Re_L = \rho_L v_j d_j/\mu_L$) is large ($Re_L = 30{,}000$). This behavior persisted over the observable length of the liquid jet (up to $75d_j$) in the absence of crossflow, similar to past observations by Mazallon et al. (1999). These results provide direct evidence that the primary breakup processes of round nonturbulent liquid jet in crossflow (shown in the following figures) are not due to the initial disturbances within the liquid jet but rather due to the aerodynamic effects of the crossflow. When viscous effects are small ($Oh < 0.1$), Mazallon et al. (1999) found that breakup regime transitions of the liquid jet are determined by the crossflow Weber number as follows: column breakup ($We_G < 4$), bag breakup ($4 < We_G < 30$) (modified by Sallam et al. (2004)), multimode breakup ($30 < We_G < 110$), and shear breakup ($110 < We_G$).

Pulsed photograph of a typical round liquid jet in uniform gaseous crossflow within the bag breakup regime is shown in Fig. 3. The ethyl alcohol jet presented herein has a jet diameter of 1 mm, crossflow (left to right) Weber number of 10, and a momentum flux ratio of 224. The image is taken at the plane of symmetry of the deflected liquid jet. The breakup process begins with the deformation of the liquid column from a circular cross-section into

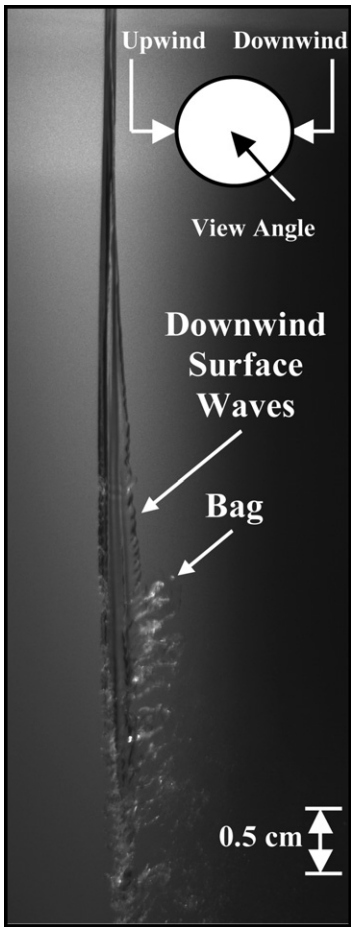

Fig. 7. Downwind surface waves of round nonturbulent liquid jets in uniform gaseous crossflow within the bag breakup regime (water jet, $d_j = 1$ mm, $We_G = 24$, and $q = 1199$).

an ellipsoidal cross-section. The deformation is caused by the reduction of gas pressure along the sides of the liquid jet as the crossflow is being accelerated over the liquid column (Aalburg et al., 2005). The increased drag force due to the now ellipsoidal cross-section enhances the tendency of the liquid column to deflect in the direction of the gas motion. Thickened regions (nodes) appear along the liquid column and define the wavelengths of column waves, λ_c, as the distance between the nodes. Bag-like structures (bags) develop between the nodes. With increasing streamwise distance along the liquid column, the bags grow progressively and its membrane eventually breaks up. This leaves the nodes connected by two thin strings very similar to the ring associated with the secondary breakup of droplets within bag breakup regime as discussed by Chou and Faeth (1998). The remaining thin liquid strings (hereby called ring) eventually breakup by Rayleigh-like breakup. At the end of the breakup process, three distinctive groups of droplets are generated: (1) relatively large droplets associated with the nodes called node-droplets, (2) ring-droplets due to the breakup of the ring, and (3) a large number of much smaller droplets called bag-droplets associated with the breakup of the membrane of the bag.

3.2. Jet surface velocity

The streamwise velocity of the liquid surface was measured by double-pulsed shadowgraphy, as shown in the inset of Fig. 4. *The nozzle exit velocity, v_j, was measured by measuring the collected volume of injected test liquid over a specific time period.* The streamwise velocity of the liquid surface, v_s, normalized by the nozzle exit velocity, v_j, is nearly unity, independent of the streamwise distance, y, traveled indicating negligible drag forces in the streamwise direction. The measurements are plotted in Fig. 4 and the standard deviation of the measurements is 6%.

3.3. Liquid column waves

The column waves involve the deflection of the entire liquid column in the cross-stream direction as was shown in Fig. 3. The wavelength, λ_c, of the column waves is defined herein as the distance between the nodes on the upwind side of the liquid jet, as shown in Fig. 3. The amplitude of the column wave grows with increasing distance in the streamwise direction of the liquid jet whereas the wavelength remains nearly constant *for a given test condition. The wavelength of the column waves was observed to vary with We_G.* This suggests that the column waves are convected along the liquid column. The column waves can be explained using Rayleigh–Taylor instability as follows: when a dense fluid is supported by a lighter fluid, the growth rate of the disturbance in case of inviscid fluids without surface tension is given by Rayleigh (1883)

$$\eta = \sqrt{gkA} \tag{1}$$

where η is the growth rate of disturbance, g is the acceleration of gravity, $k = 2\pi/\lambda$ is the wave number, λ is the wavelength, $A = (\rho_2 - \rho_1)/(\rho_2 + \rho_1)$ is the Atwood number, and ρ_1 and ρ_2 are the densities of the lighter and heavier fluids, respectively. Eq. (1) shows that the growth rate will increase with the increase in the wave number. The effects of surface tension and uniform rotation on the growth rate of Rayleigh–Taylor instabilities for two-fluid system were analytically investigated by El-Ansary et al. (2002) where the growth rate of two-fluid systems accelerated by gravity was given by

$$\frac{\eta^2}{b} = g\left[\frac{\rho_2 - \rho_1}{\rho_2 + \rho_1} - \frac{k^2\sigma}{g(\rho_2 + \rho_1)}\right], \quad b^2 = \frac{k^2\eta^2}{4\Omega^2 + \eta^2} \tag{2}$$

where Ω is the angular velocity of the rotation. Neglecting the effect of rotation, then $b = k$, and Eq. (2) simplifies to

$$\eta^2 = kg\frac{\rho_2 - \rho_1}{\rho_2 + \rho_1} - \frac{k^3\sigma}{\rho_2 + \rho_1} \tag{3}$$

When the fluid layers were accelerated by air pressure rather than gravity, similar behavior was observed by Taylor (1950).

To estimate the acceleration of the liquid jet, a, due to the gaseous crossflow, one can approximate the drag force

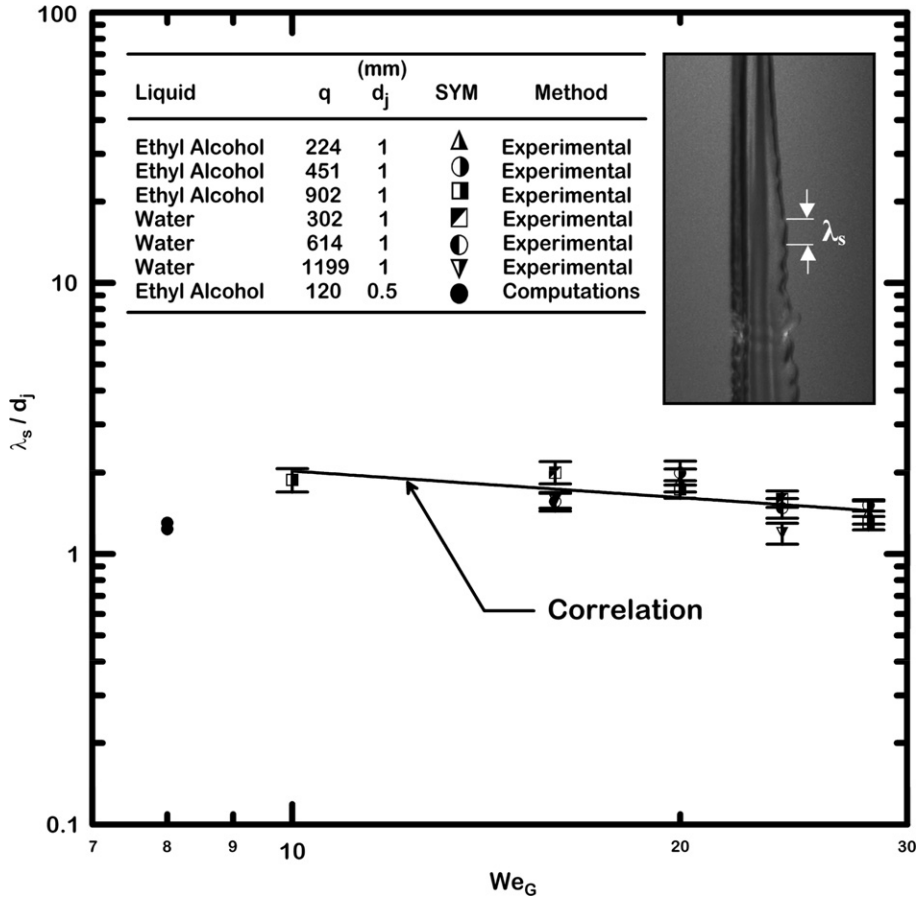

Fig. 8. Wavelengths of downwind surface waves as a function of crossflow Weber number.

acting on the liquid jet as a drag force acting on a cylinder in a crossflow. The drag force, F, acting on a cylindrical liquid jet element with a height L, could then be approximated as

$$F = C_D\left(\frac{1}{2}\rho_G U_G^2\right)(d_j L) = \left(\rho_L \frac{\pi}{4} d_j^2 L\right)a \tag{4}$$

where C_D is the drag coefficient. Rearranging Eq. (4) and assuming that the liquid jet remains normal to the crossflow, the acceleration of a liquid jet in crossflow can be approximated as

$$a = \frac{2C_D\rho_G|v|_G^2}{\pi\rho_L d_j} \tag{5}$$

Substitute Eq. (5) into Eq. (3) and setting ($g = a$) yields

$$\eta^2 = k\frac{2C_D\rho_G|v|_G^2}{\pi\rho_L d_j}\frac{\rho_L - \rho_G}{\rho_L + \rho_G} - \frac{k^3\sigma}{\rho_L + \rho_G} \tag{6}$$

For liquid jet in gaseous crossflow, $\rho_L \gg \rho_G$. Therefore, Eq. (6) can be written as

$$\eta = \left[k\frac{2C_D\rho_G|v|_G^2}{\pi\rho_L d_j} - \frac{k^3\sigma}{\rho_L}\right]^{1/2} \tag{7}$$

For a cylinder in crossflow, the drag coefficient, $C_{D,cylinder}$, depends on the crossflow Reynolds number ($Re_G = \rho_G U_G d_j/\mu_G$) and is given by White (1991)

$$C_{D,cylinder} \approx 1 + 10Re_G^{-2/3}; \quad 1 < Re_G < 2\times 10^5 \tag{8}$$

For the range of crossflow Reynolds numbers considered in the present study ($793 < Re_G < 2456$), the drag coefficient can e approximated as 1.0 and the growth rate of Rayleigh–Taylor instabilities as a function of the wave number can be obtained from Eq. (7) as shown in Fig. 5. The test conditions in Fig. 5 include: (a) water liquid jet with nozzle exit diameter of 1 mm and crossflow Weber number of 8 with and without the effect of surface tension, and (b) ethyl alcohol liquid jet with nozzle exit diameter of 1 mm and crossflow Weber number of 28 with and without the effect of surface tension. The results show that the presence of surface tension damps the Rayleigh–Taylor instabilities growth at high wave numbers.

To find the wave number corresponding to the maximum growth rate, one can differentiate Eq. (8) as follows:

$$\frac{d\eta}{dk} = \frac{\left(\frac{2C_D\rho_G|v|_G^2}{\pi\rho_L d_j} - \frac{3\sigma}{\rho_L}k^2\right)}{2\left(\frac{2C_D\rho_G|v|_G^2}{\pi\rho_L d_j}k - \frac{\sigma}{\rho_L}k^3\right)^{1/2}} \tag{9}$$

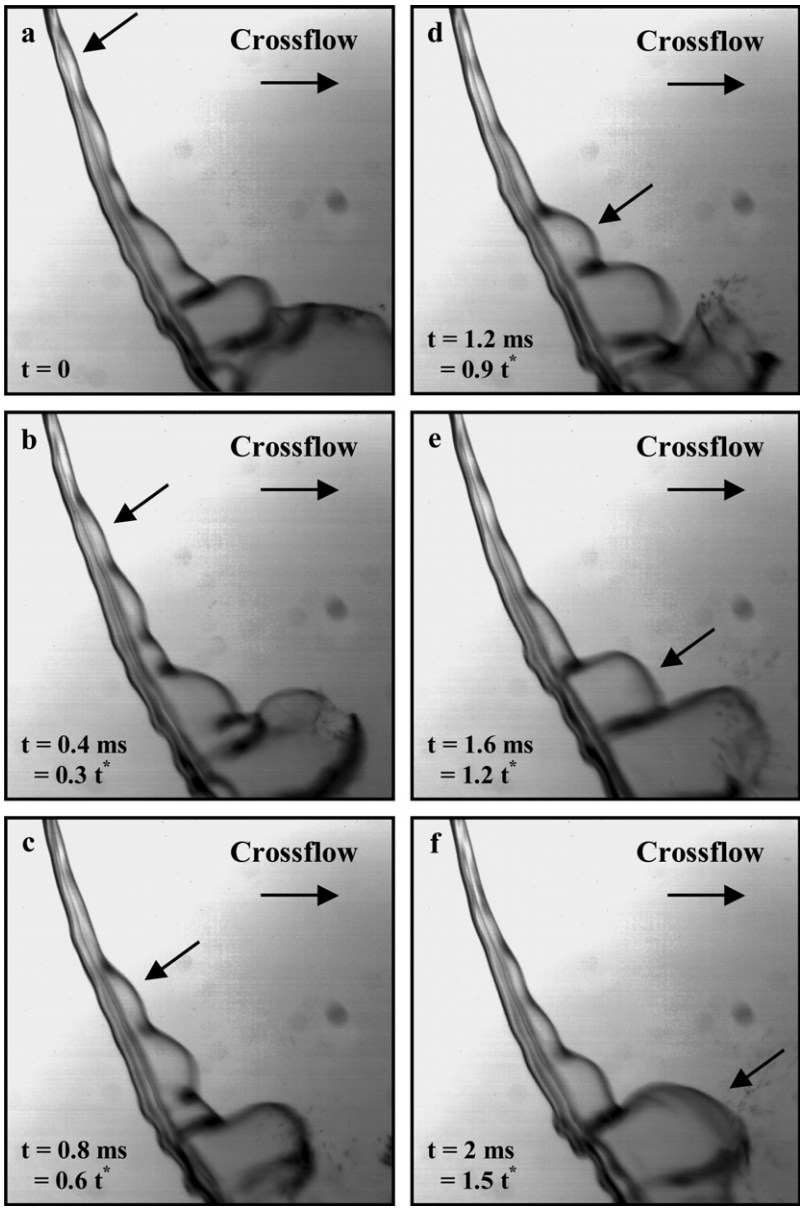

Fig. 9. Formation and breakup of bags (water jet, $d_j = 1$ mm, $We_G = 8$, and $q = 97$).

At the maximum growth rate $d\eta/dk = 0$ which yields

$$k^2 = \frac{2C_D}{3\pi}\frac{\rho_G|v_G|^2}{\sigma}\frac{1}{d_j} \tag{10}$$

Substituting the wave number ($k = 2\pi/\lambda_c$) and the crossflow Weber number in Eq. (10) yields

$$\frac{\lambda_c}{d_j} = C_\lambda\sqrt{\frac{6\pi^3}{C_D}}We_G^{-0.5} \tag{11}$$

where C_λ is an empirical parameter of order of unity. The present measurements of the wavelengths of column waves for various test conditions are plotted as suggested by Eq. (11) in Fig. 6. The present measurements have maximum uncertainties of 9.9% (95% confidence). The measurements of Mazallon et al. (1999) and the computational prediction of column waves (Ng et al., submitted for publication) within the column and bag breakup regimes are also shown in Fig. 6. The present measurements agree with the experimental results of Mazallon et al. (1999) within experimental uncertainties. Note that Mazallon et al. (1999) fitted a single correlation across the column, bag, and multimode breakup regimes. The data point in the multimode breakup regime did post an acute effect to Mazallon et al. (1999) correlation. The best fit correlation of the present measurements within the bag breakup regime is given by

$$\frac{\lambda_c}{d_j} = 5.3We_G^{-0.26} \tag{12}$$

The correlation coefficient of the fit is 0.62. The power of the crossflow Weber number in Eq. (12) is not −0.5 as

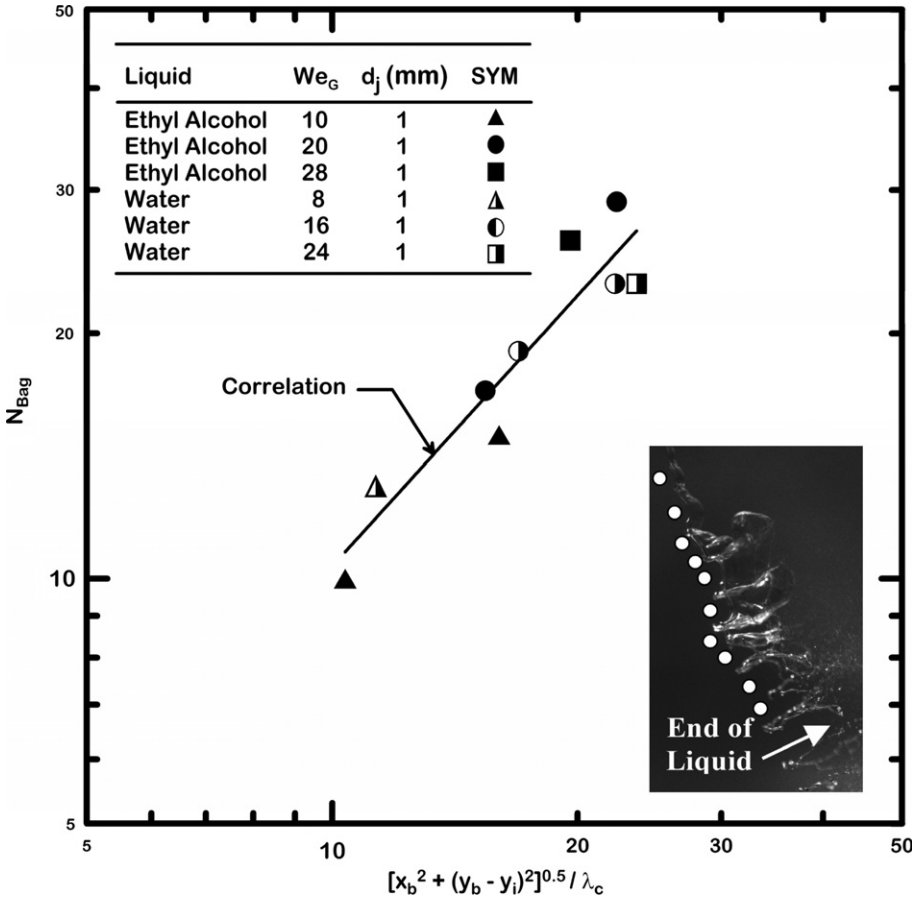

Fig. 10. The number of bags along the liquid column.

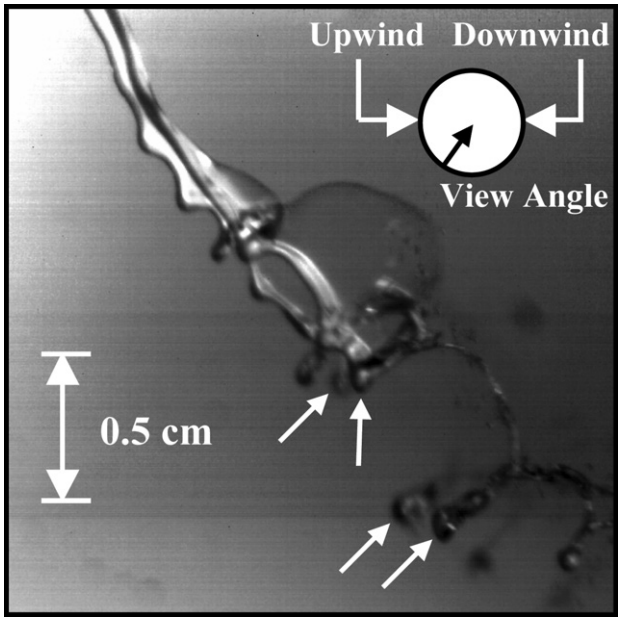

Fig. 11. Typical 4-nodes bag (water jet, $d_j = 1$ mm, $We_G = 8$, and $q = 65$).

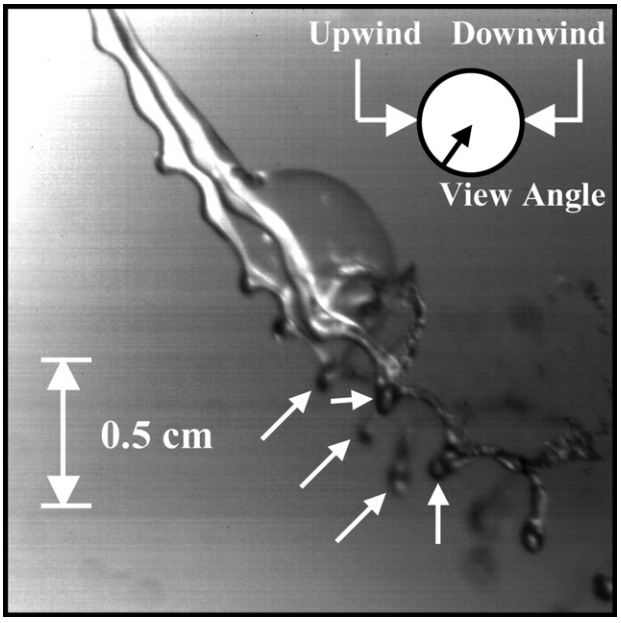

Fig. 12. Typical 5-nodes bag (water jet, $d_j = 1$ mm, $We_G = 8$, and $q = 65$).

suggested by Eq. (11), but the difference is not large in view of the approximations used to find Eq. (11) and *the* experimental uncertainties. Present measurements are also correlated as suggested by Eq. (11) in Fig. 6 yielding the following theoretical fit:

$$\frac{\lambda_c}{d_j} = 9.7 We_G^{-1/2} \tag{13}$$

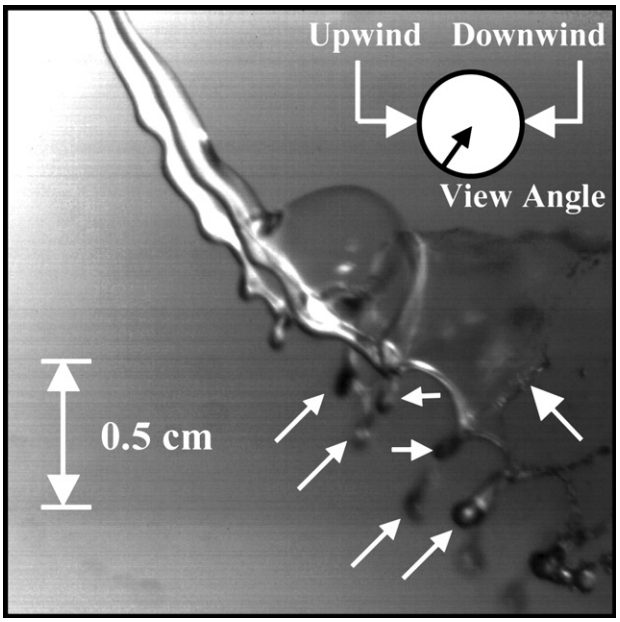

Fig. 13. Typical 6-nodes bag (water jet, $d_j = 1$ mm, $We_G = 8$, and $q = 65$).

The correlation coefficient of the fit is 0.56. For the range of present measurements, the average C_D can be estimated by Eq. (8) as 1.08. The empirical parameter, C_λ, can then be computed by comparing Eq. (11) and (13) as

$$C_\lambda \sqrt{\frac{6\pi^3}{C_D}} = 9.7 \tag{14}$$

resulting in a value of $C_\lambda = 0.7$, which is of order of unity. The reasonable value of the empirical coefficient, C_λ, and the fact that the wavelength of column waves was independent of the momentum flux ratio *for the present test conditions as shown* in the legend of Fig. 6 further support the present claim that the column waves within the bag breakup regime are convected along the liquid jet and are caused by Rayleigh–Taylor instabilities.

3.4. Downwind surface waves

A remarkable feature of liquid jet breakup in crossflow is the surface waves appearing along the downwind surface of the liquid column. To the authors' knowledge these surface waves were not reported before in the literature. To obtain this view of downwind surface waves the camera was tilted 40° in the downwind direction from the normal position to the crossflow, as shown in the inset of Fig. 7. The downwind surface waves are shown in Fig. 7 (and also in the inset of Fig. 8) for the following test condition: Water liquid jet with nozzle exit diameter of 1 mm, crossflow Weber number of 24, and a momentum flux ratio of

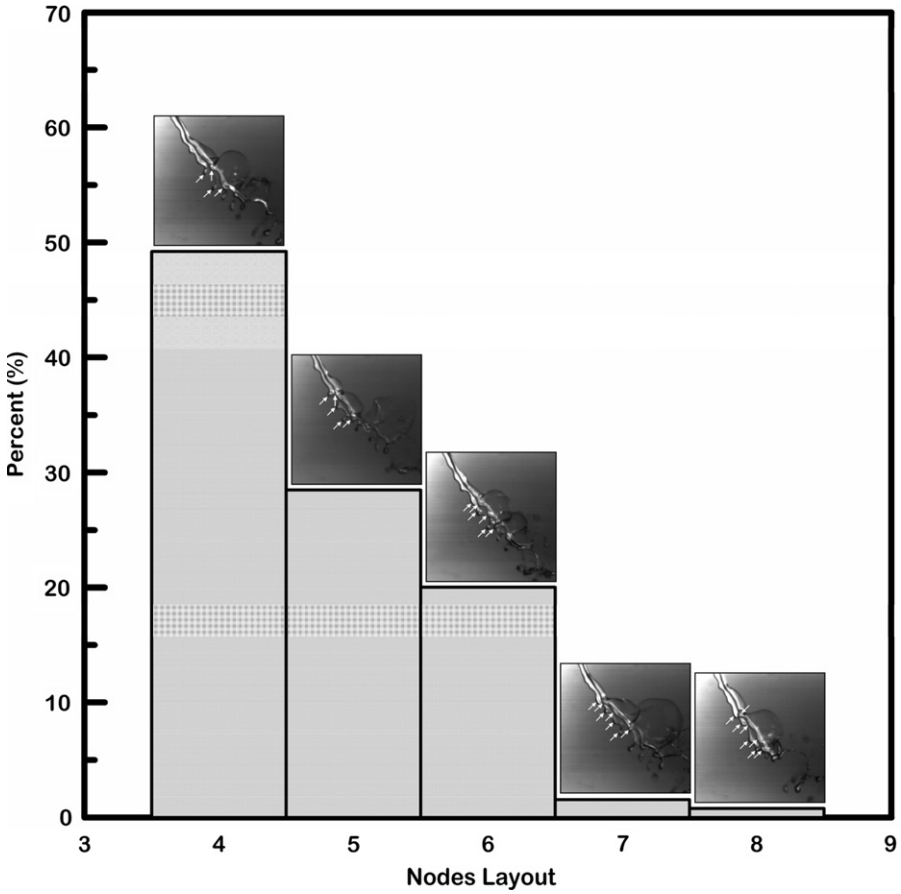

Fig. 14. Nodes layout frequency distribution (water jet, $d_j = 1$ mm, $We_G = 8$, and $q = 65$).

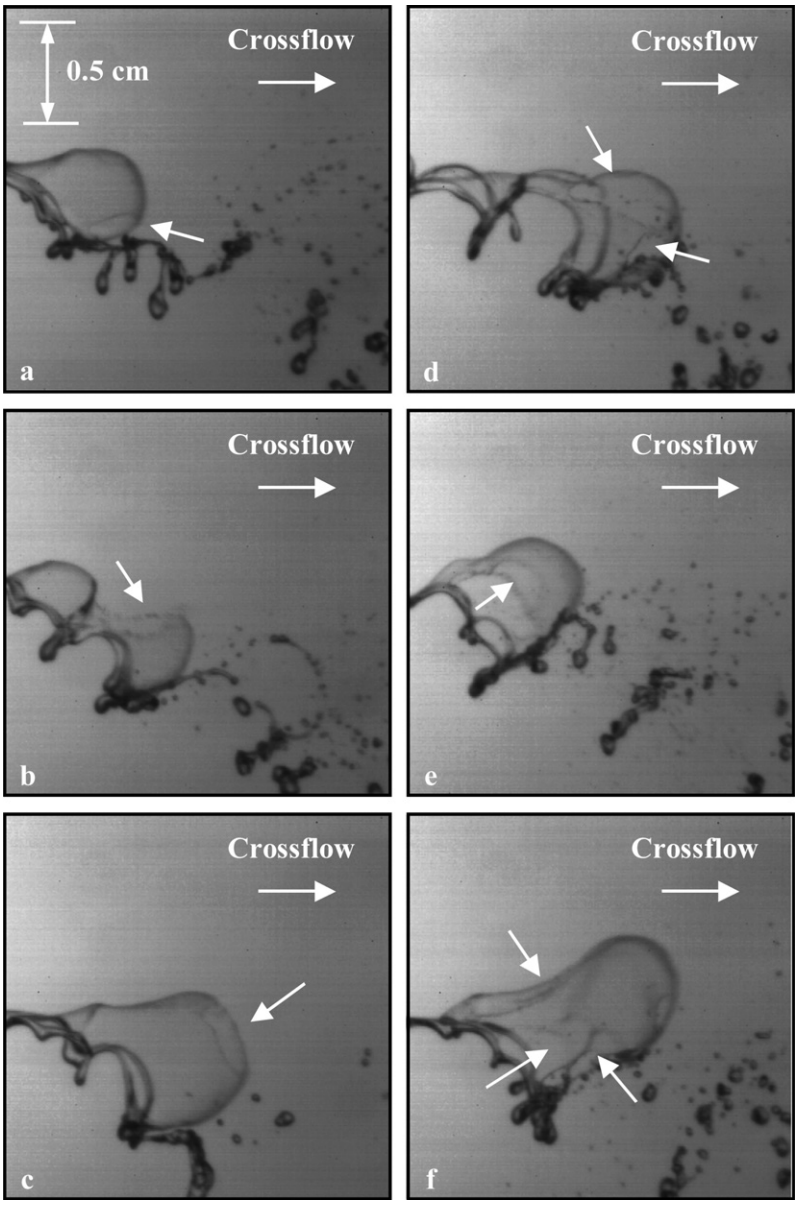

Fig. 15. The location of the onset of breakup of the bag membrane (water jet, $d_j = 1$ mm, $We_G = 8$, and $q = 32$).

1199. *These downwind surface waves were observed on the surface of the liquid jet for the following range of test conditions: crossflow Weber number between* 10 *and* 30 *and momentum flux ratio between* 220 *and* 1200.

The wavelength of the downwind surface waves, λ_s, is defined as the distance between troughs of the surface waves on the downwind side of the liquid jet, as shown in the inset of Fig. 8. The wavelengths of the downwind surface waves for various test conditions, along with the computational results of Ng et al. (submitted for publication) are plotted against the Crossflow Weber number in Fig. 8. The best fit correlation of the present measurements is given by

$$\lambda_s/d_j = 4.3(We)^{-0.33} \tag{15}$$

The correlation coefficient of the fit is 0.61. The downwind surface waves were observed to originate near the sides of the liquid column where the velocities of the gaseous crossflow are higher than in any other region on the jet surface. This suggests that these waves are associated with aerodynamic effects but the exact mechanism for their formation is still to be explored.

3.5. Bag formation

High-speed imaging was used to observe the development of column waves into bags as shown in Fig. 9 for the following test conditions: water jet with a nozzle exit diameter of 1 mm, crossflow (left to right) Weber number of 8, and a momentum flux ratio of 97. The region shown in Fig. 9 corresponds to the onset of the bag formation and the images were taken at the plane of symmetry of the deflected liquid jet for incremental time of $0.3t^*$ where t^*

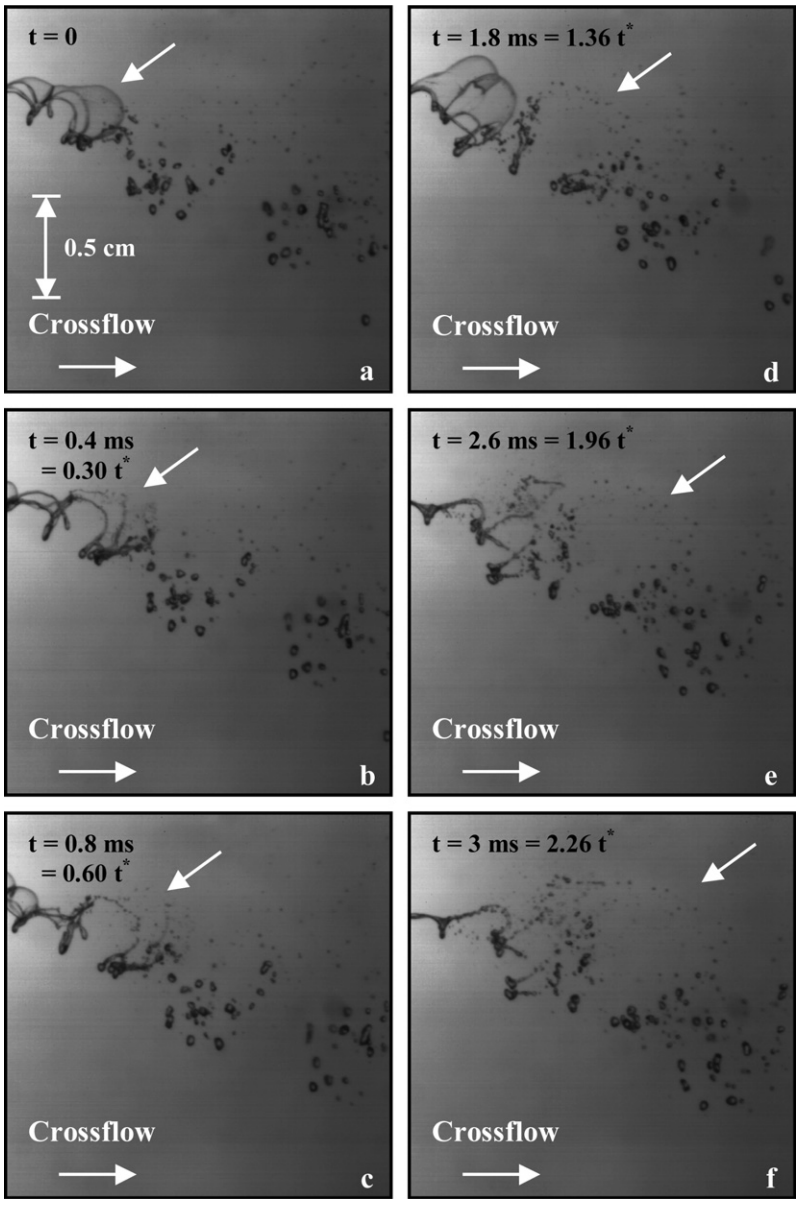

Fig. 16. Ring breakup (water jet, $d_j = 1$ mm, $We_G = 8$, and $q = 32$).

is the Ranger and Nicholls (1969) aerodynamic characteristic time. The column wave is observed to grow with the streamwise distance. The high pressure produced by the stagnating gas on the upwind side of the flattened liquid column causes the deformation of the central portion of the liquid column into a bag.

The number of bags along the liquid jet, N_B, was measured as follows: the first bag is identified when the ratio of liquid jet cross-stream diameter, d_s, to the nozzle exit diameter, dj, between two adjacent nodes is greater than one and the last bag along the liquid jet is associated with the end of the liquid column. The number of bags can be calculated by approximating the liquid column between the onset of bag formation and the end of the liquid column as a straight line with a length of L_s and dividing it by the wavelength of column waves, λ_c, as follows:

$$N_B \sim \frac{L_s}{\lambda_c} = C_b \frac{\sqrt{x_b^2 + (y_b - y_{bf})^2}}{\lambda_c} \tag{16}$$

where C_b is an empirical parameter of order of unity, y_{bf} is the measured height of the jet at the onset of bag formation, y_b is the measured height of jet at the end of the liquid column, x_b is the measured cross-stream distance from the axis of the nozzle to the end of the liquid column, *and* λ_c *is the column wave length corresponding to the particular* We_G (λ_c *varies with* We_G as discussed in Section 3.3) at which the number of bags (N_B) *is measured*. The number of bags was measured for various test conditions and plotted in Fig. 10

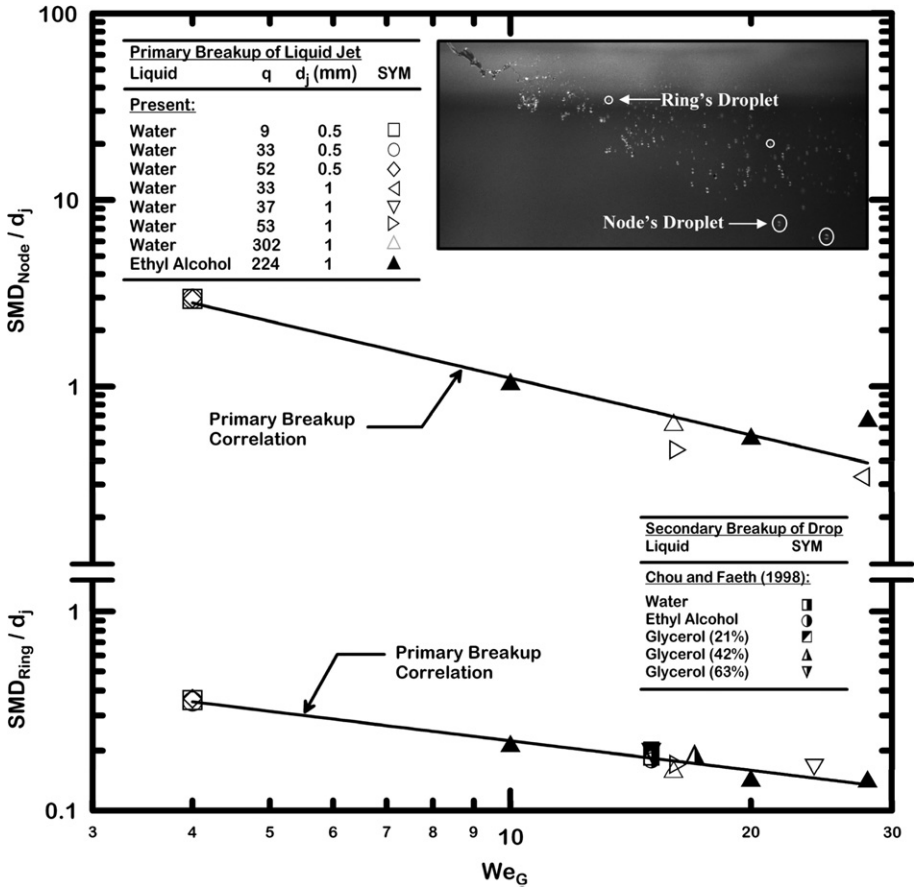

Fig. 17. The sizes of node-droplets and ring-droplets as function of the crossflow Weber number.

as suggested by Eq. (16). The best fit correlation for the present measurements is given by

$$N_B = 0.82\left(\frac{[x_b^2 + (y_b - y_{bf})^2]^{0.5}}{\lambda_c}\right)^{1.1} \quad (17)$$

The correlation coefficient of the fit is 0.94. The coefficient and the power of the fit in Eq. (17) are close to unity, as suggested by Eq. (16).

3.6. Nodes layout

The number of nodes observed per one bag was typically 4–8 nodes. Photographs of four-nodes, five-nodes, and six-nodes layouts are shown in Figs. 11–13, respectively, for a water jet with a nozzle exit diameter of 1 mm, crossflow Weber number of 8, and a momentum flux ratio of 65. These photographs were taken by tilting the camera 77° in the upstream direction from the normal to the plane of symmetry of the deflected liquid jet as shown in the inset of Fig. 11. The span-wise distance between the nodes was observed to increase in the streamwise direction. The probability of occurrence of multiple nodes layouts for *this test condition* is plotted in Fig. 14, where 49% of the bags had 4-node layout, 28% had 5-node layout, and 20% had 6-nodes layout. Rarely, 7-nodes layout and 8-nodes layout were observed and represented approximately 2% and 1% of total occurrences, respectively.

3.7. Breakup of the bag membrane

As the bag is convected in the streamwise direction, its size grows progressively and the thickness of its membrane becomes smaller. Eventually the thin membrane breaks up after the bag reaches a maximum size. The membrane breakup is shown in Fig. 15 for the following test conditions: water jet with a nozzle exit diameter of 1 mm, crossflow (left to right) Weber number of 8, and a momentum flux ratio of 32. In Fig. 15 the bag membrane is *shown* to start breaking at: (a) the bottom side (42% occurrences), (b) the top side (10% occurrences), (c) the center (15% occurrences), (d) the top and bottom sides (27% occurrences), (e) the two sides (4% occurrences), and (f) the top and bottom and the two sides (2% occurrences).

The bottom side of the bag is typically stretched in the span-wise direction more than top side and consequently the membrane tends to break from the bottom side. The number of nodes per bag affected the breakup mechanism as follows: the breakup of the membrane typically starts from the bottom and continue uninterrupted for 4-nodes and 5-nodes bags. However for 6-nodes bags, as shown in Fig. 13, the bag typically opens from the bottom, stops

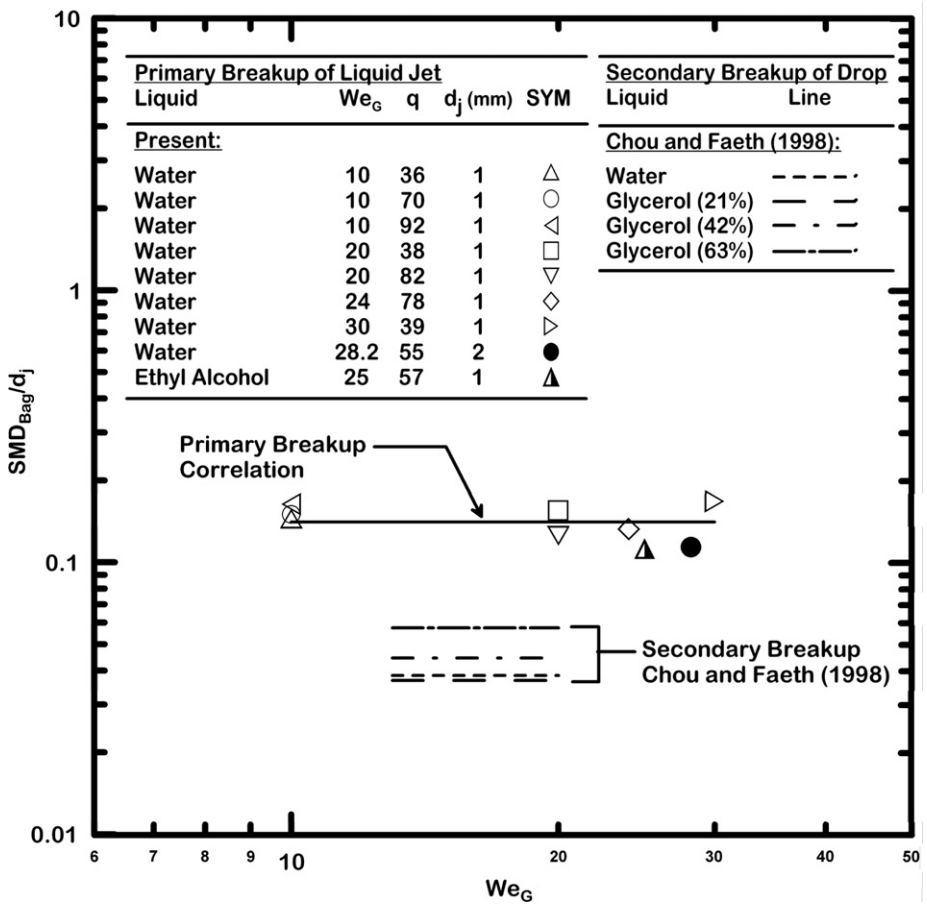

Fig. 18. The sizes of bag-droplets as function of the crossflow Weber number.

momentarily on the string of liquid connecting the two intermediate nodes, before completely breaks up. The breakup of the membrane results in a large number of very small droplets (bag-droplets).

3.8. Ring breakup

After the breakup of the bag membrane the remaining part of the bag; the ring, breaks up similar to the ring breakup of secondary breakup of droplets (Chou and Faeth, 1998). The ring breakup of a typical round nonturbulent liquid jet in uniform gaseous crossflow is shown in Fig. 16 for a water jet with a nozzle exit diameter of 1 mm, crossflow (left to right) Weber number of 8, and a momentum flux ratio of 32. The breakup starts when the nodes evolve into ligaments (Fig. 16b). The two strings of the ring breakup (Fig. 16c) forming small droplets (ring-droplets) while the ligaments breakup (Fig. 16d) into relatively large droplets (node-droplets). At the end of the ring breakup (Fig. 16f) a poly-dispersed array of drops is formed from *the* node-droplets and the ring-droplets.

3.9. Droplets sizes

The size measurements of node-droplets and ring-droplets are plotted as SMD vs. the crossflow Weber number in Fig. 17. Also included in Fig. 17 the measurements of ring-droplets for the secondary breakup of drops by Chou and Faeth (1998). The best fit correlations for the present measurements are as follows:

$$\mathrm{SMD}_{\mathrm{node}}/d_j = 11.4We^{-1.0} \tag{18}$$

$$\mathrm{SMD}_{\mathrm{ring}}/d_j = 4.8We^{-1.0} \tag{19}$$

The correlation coefficients of the fits are 0.96 and 0.98, for the node- and the ring-droplets, respectively. The sizes of the node- and the ring-droplets decrease with increasing crossflow Weber number. The present measurements for ring-droplets are similar to previous measurements of ring-droplets of the secondary breakup of drops.

The size measurements of bag-droplets are plotted as SMD vs. crossflow Weber number in Fig. 18. Also included in Fig. 18 are the correlations of the Chou and Faeth (1998) for the secondary breakup of drops. The best fit correlation of the present measurements is given by

$$\mathrm{SMD}_{\mathrm{bag}}/d_j \approx 0.14 \tag{20}$$

The standard deviation of the measurements is 15%. The size of the bag-droplets is independent of the crossflow Weber number suggesting that the membrane breakup is triggered when the thickness of the bag membrane reaches a certain minimum value. The sizes of the bag-droplets in the present study are larger than those of the secondary breakup of

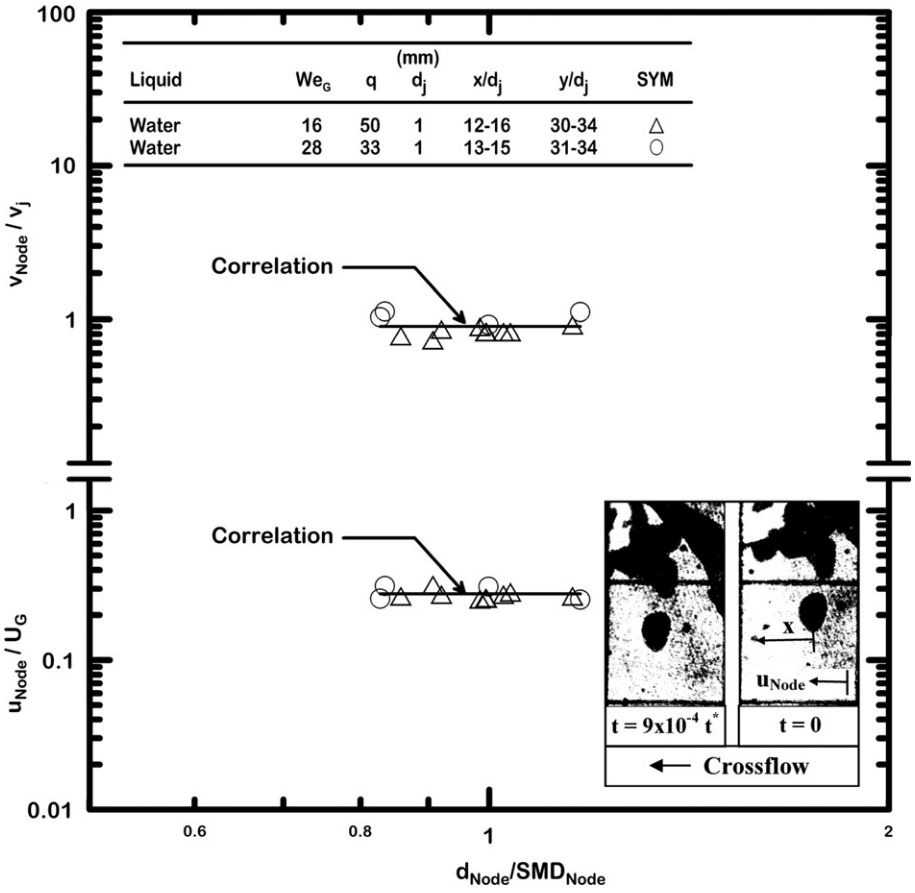

Fig. 19. The streamwise and cross-stream velocities of the node-droplets as a function of node-droplets sizes.

drops within the (Chou and Faeth, 1998). This may be due to the complex membrane breakup process in the case of liquid jet breakup compared to the symmetric membrane breakup in the secondary breakup of liquid drops.

3.10. Droplets velocities

Droplet velocities are a function of time and position. In this section the droplet velocities right after breakup is reported. The cross-stream and streamwise velocities of the node-droplets, u_{node} and v_{node}, as a function of droplets sizes are shown in Fig. 19. The inset of Fig. 19 shows a typical double pulse shadowgraphs used to measure the droplets velocities. The velocities are nearly independent of droplets sizes, *within experimental uncertainties*, and are given by

$$\frac{u_{\text{node}}}{U_{\text{G}}} \approx 0.28 \tag{21}$$

$$\frac{v_{\text{node}}}{v_j} \approx 0.9 \tag{22}$$

The standard deviations of the measurements are 8% and 14%, for cross-stream and streamwise velocities, respectively. The cross-stream and streamwise velocities of the ring-droplets, u_{ring} and v_{ring}, as a function of droplets sizes are shown in Fig. 20. The velocities are nearly independent of drop sizes, *within experimental uncertainties*, and are given by

$$\frac{u_{\text{ring}}}{U_{\text{G}}} \approx 0.27 \tag{23}$$

$$\frac{v_{\text{ring}}}{v_j} \approx 0.87 \tag{24}$$

The standard deviations of the measurements are 17% and 12%, for cross-stream and streamwise velocities, respectively. The cross-stream and streamwise velocities of the bag-droplets, u_{bag} and v_{bag}, as a function of bag-droplet size after the breakup of the bag membrane are shown in Fig. 21. The streamwise and cross-stream velocities of the bag-droplets are independent of the droplets sizes, *within experimental uncertainties*, and are given by

$$\frac{u_{\text{bag}}}{U_{\text{G}}} \approx 0.34 \tag{25}$$

$$\frac{v_{\text{bag}}}{v_j} \approx 0.56 \tag{26}$$

The standard deviations of the measurements are 32% and 72% for cross-stream and streamwise velocities, respectively. The large standard deviations of the velocities of the bag-droplets may be attributed to the violent nature of the breakup of the bag membrane. The upwind surface of the bag membrane is expected to have higher pressure

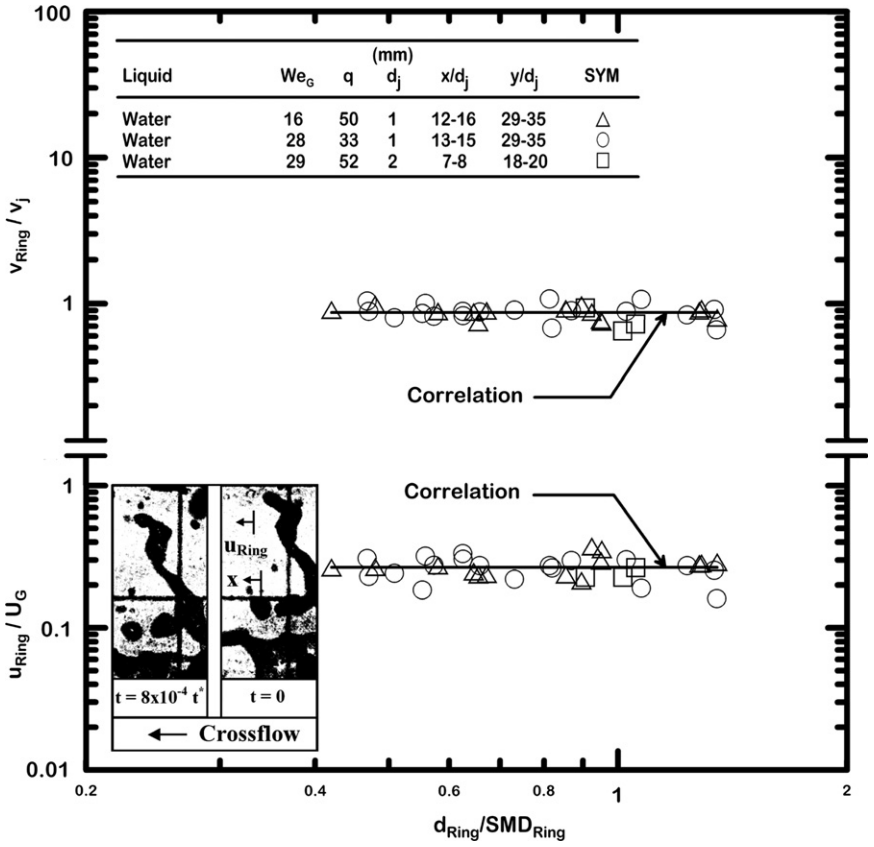

Fig. 20. The streamwise and cross-stream velocities of the ring-droplets as a function of ring-droplets sizes.

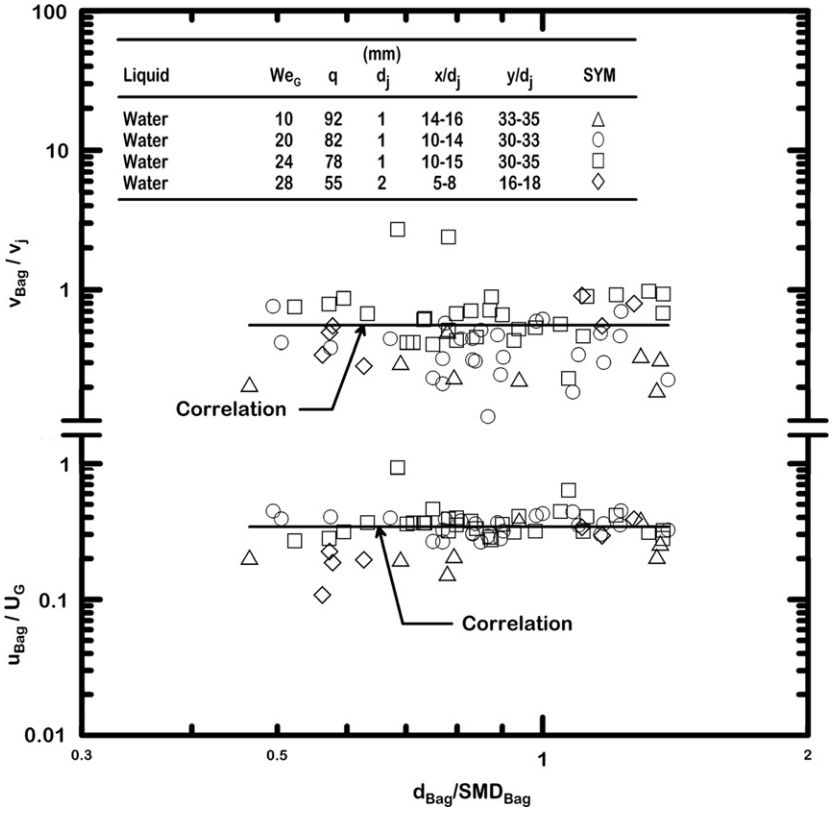

Fig. 21. The streamwise and cross-stream velocities of the bag-droplets as a function of bag-droplets sizes.

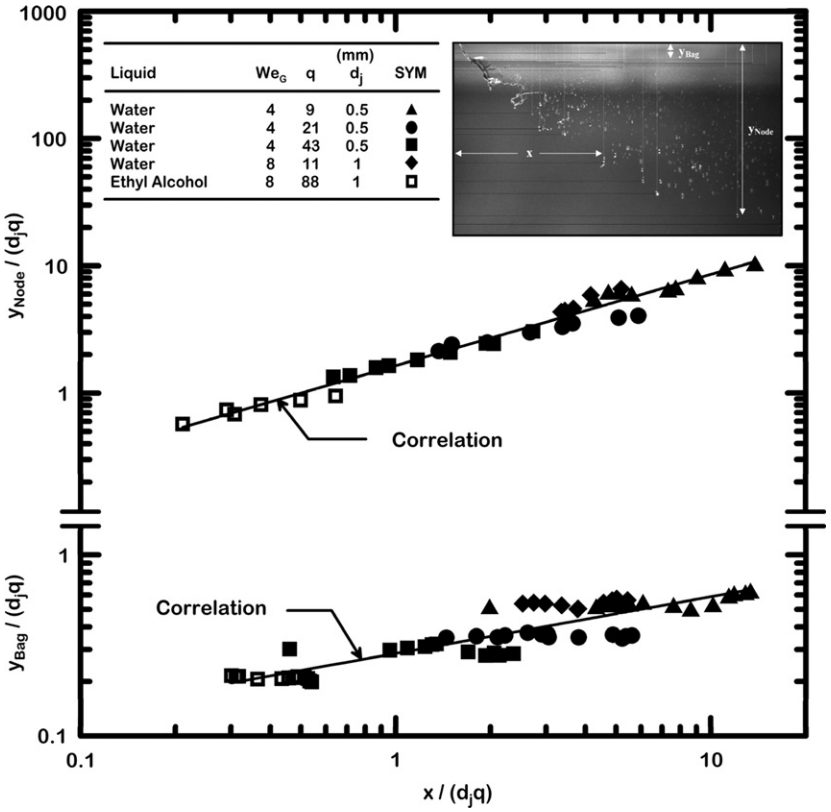

Fig. 22. The trajectories of node-droplets and bag-droplets.

than its downwind surface due to aerodynamic drag forces. This high pressure would result into a burst of bag-droplets in the direction of the membrane breakup. The seemingly random openings of the membrane (bottom, center, top) would possibly result in large streamwise and cross-stream velocities variations for the bag-droplets. The bag-droplets traveled with higher cross-stream velocities but with lower streamwise velocities compared to the node- and ring-droplets. This difference may be attributed to the combined effects of the smaller relaxation time of the smaller bag-droplets and the high pressure produced by the stagnating gas on the upwind side of the membrane *that upon* bursting of the membrane propels the bag-droplets in the cross-stream directions.

3.11. Droplets trajectories

The trajectories of node-droplets and bag-droplets for various test conditions are shown in Fig. 22 where x is the cross-stream distance from the center of the liquid jet, and y represents the streamwise distance (height) from the nozzle exit. The best fit correlations of the present measurements are given by

$$y_{\text{node}}/(d_j q) = 1.64[x/(d_j q)]^{0.72} \quad (27)$$

$$y_{\text{bag}}/(d_j q) = 0.82[x/(d_j q)]^{0.63} \quad (28)$$

The correlation coefficients of the fits are 0.98 and 0.89 for node- and bag-droplets, respectively. The node-droplets penetrated the crossflow with a steeper trajectory than a liquid jet within the bag breakup regime (Sallam et al., 2004). This is because the hemispherical-shaped liquid jet has larger drag coefficient due to the presence of the bags than the spherical-shaped droplets, resulting in the latter to show a steeper trajectory. *Moreover, when comparing the trajectories for node-droplets and bag-droplets, there exist distinct trajectories for the bag-droplets and the node-droplets due to the faster relaxation time of the relatively smaller bag-droplets and the higher inertia of the relatively larger node-droplets*. This natural size sorting mechanism could have practical applications in developing techniques to generate monodispersed sprays.

4. Conclusions

The investigation involved measurements of the wave phenomena and the breakup properties of round nonturbulent liquid jets in uniform gaseous crossflow within the bag breakup regime. Test conditions were limited to pressure-fed supercavitating nozzles of 0.5 mm, 1 mm, and 2 mm, water and ethyl alcohol as the test liquids, crossflow Weber numbers (4–29), momentum flux ratio (9–1199) and small *Oh* number (<0.1). The major conclusions are as follows:

1. Two waves were observed in the present study: (a) column waves were observed to be convected along the liquid jet with a constant jet streamwise velocity and

nearly constant wavelength and were attributed to Rayleigh–Taylor instability and (b) downwind surface waves were observed to develop on the downwind surface of the liquid column near its two sides. The wavelength of the surface waves decreases as the crossflow Weber number increases.

2. Earlier correlation of the wavelength of column waves due to Mazallon et al. (1999) provides a reasonable correlation of existing measurements for We_G of 2–30. This correlation, however, is influenced by effects of transition to multimode breakup at large We_G and column breakup at small We_G which provides an explanation for the somewhat stronger dependence of the wavelength of the column waves by Mazallon et al. (1999) correlation than the present correlation for the bag breakup, Eq. (12).
3. The column waves evolve into bag-like structures (bags) due to the high pressure produced by the stagnating gas on the upwind side of the flattened liquid column. The bags were observed to have multiple nodes along their rings, with 4-nodes and 6-nodes typically observed. The bag size progressively increases as it is convected in the streamwise direction and its bottom side is stretched in the span-wise direction more than its top side causing its membrane to typically breakup from the bottom.
4. The bag breakup results in three distinctive droplets sizes as follows: (a) very small droplets due to the breakup of the bag membrane, (b) small droplets due to the breakup of the two strings of the ring, and (c) large droplets associated with the nodes. The sizes of the node- and ring-droplets are inversely proportional to the crossflow Weber number (We_G) whereas the size of the bag-droplets is constant.
5. The bag-droplets immediately after breakup traveled with higher cross-stream velocities but lower streamwise velocities than the node- and the ring-droplets due to the high pressure produced by the stagnating gas on the upwind side of the bags that upon bursting propels the bag-droplets in the cross-stream directions. The bag-droplets then travel into a separate trajectory than the relatively larger node-and ring-droplets.

Acknowledgements

This research was sponsored by Oklahoma NSF EPSCoR under Grant No. EPS-0132534. The authors would like to thank Dr. C. Aalburg for the valuable discussion of the present work.

References

Aalburg, C., van Leer, B., Faeth, G.M., Sallam, K.A., 2005. Properties of nonturbulent round liquid jets in uniform gaseous crossflows. Atomization Spray 15, 271–294.

Becker, J., Hassa, C., 2002. Breakup and atomization of a kerosene jet in crossflow at elevated pressure. Atomization Spray 12, 49–67.

Bellofiore, A., Cavaliere, A., Ragucci, R., 2007. Air density effect on the atomization of liquid jets in crossflow. Combust. Sci. Tech. 179, 319–342.

Birouk, M., Azzopardi, B.J., Stabler, T., 2003. Primary break-up of a viscous liquid jet in a cross airflow. Part. Part. Syst. Char. 20, 283–289.

Birouk, M., Iyogun, C.O., Popplewell, N., 2007. Role of viscosity on trajectory of liquid jets in a cross-airflow. Atomization Spray 17, 267–287.

Cavaliere, A., Ragucci, R., Noviello, C., 2003. Bending and break-up of a liquid jet in a high pressure airflow. Exp. Therm. Fluid Sci. 27, 449–454.

Chou, W.-H., Faeth, G.M., 1998. Temporal properties of secondary drop breakup in the bag breakup regime. Int. J. Multiphase Flow 24, 889–912.

El-Ansary, N.F., Hoshoudy, G.A., Abd-Elrady, A.S., Ayyad, H.A., 2002. Effects of surface tension and rotation on the Rayleigh–Taylor instability. Phys. Chem. Chem. Phys. 4, 1464–1470.

Geary, E.L., Margettes, M.J., 1969. Penetration of a high velocity gas stream by a water jet. J. Spacecraft 6, 79–81.

Inamura, T., 2000. Trajectory of a liquid jet traversing subsonic airstreams. J. Propul. Power 16, 155–157.

Iyogun, C.O., Birouk, M., Popplewell, N., 2006. Trajectory of water jet exposed to low subsonic cross-flow. Atomization Spray 16, 963–979.

Kitamura, Y., Takahashi, T., 1976. Stability of a liquid jet in air flow normal to the jet axis. J. Chem. Jpn. 9, 282–286.

Less, D.M., Schetz, J.A., 1986. Transient behavior of liquid jets injected normal to a high-velocity gas stream. AIAA J. 24, 1979–1985.

Madabhushi, R.K., 2003. A model for numerical simulation of breakup of a liquid jet in crossflow. Atomization Spray 13, 413–424.

Mazallon, J., Dai, Z., Faeth, G.M., 1999. Primary breakup of nonturbulent round liquid jets in gas crossflows. Atomization Spray 9, 291–311.

Ng, C.-L., Sallam, K.A., Aalburg, C., Metwally, H.M., submitted for publication. Deformation of round nonturbulent liquid jets in crossflow. Atomization Spray.

Nguyen, T.T., Karagozian, A.R., 1992. Liquid fuel jet in subsonic crossflow. J. Prop. Power 8, 21–29.

Ragucci, R., Bellofiore, A., Cavaliere, A., 2007. Trajectory and momentum coherence breakdown of a liquid jet in high-density air cross-flow. Atomization Spray 17, 47–70.

Ranger, A.A., Nicholls, J.A., 1969. The aerodynamic shattering of liquid drops. AIAA J. 7, 285–290.

Rayleigh, J.W.S., 1883. Investigation of the character of the equilibrium of an incompressible heavy fluid of variable density. Proc. London Math. Soc. 14, 170–177.

Ryan, M.J., 2006. CFD prediction of the trajectory of a liquid jet in a non-uniform air crossflow. Comput. Fluids 35, 463–476.

Sallam, K.A., Aalburg, C., Faeth, G.M., 2004. Breakup of round nonturbulent liquid jets in gaseous crossflows. AIAA J. 42, 2529–2540.

Schetz, J.A., Padhye, A., 1977. Penetration and breakup of liquids in subsonic airstreams. AIAA J. 15, 1385–1390.

Stenzler, J.N., Lee, J.G., Santavicca, D.A., Lee, W., 2006. Penetration of liquid jets in a cross-flow. Atomization Spray 16, 887–906.

Taylor, G.I., 1950. The instabilities of liquid surfaces when accelerated in a direction perpendicular to their planes. I. Proc. R. Soc. London Ser. A 201, 192–196.

Vich, G., 1997. Destabilisation d'un Jet Liquide par un Ecoulement Gazeux Perpendiculaire. Ph.D. Dissertation. University of Rouen, Rouen.

White, F.M., 1991. Viscous Fluid Flow. Mc-Graw-Hill, Inc.

Wu, P.-K., Kirkendall, K.A., Fuller, R.F., Nejad, A.S., 1997. Breakup processes of liquid jets in subsonic crossflows. J. Prop. Power 13, 64–73.